PERGAMON

International Journal of Multiphase Flow 27 (2001) 949–970

International Journal of Multiphase Flow

www.elsevier.com/locate/ijmulflow

Structure of a swirling, recirculating coaxial free jet and its effect on particle motion

Ryan B. Wicker [a,*], John K. Eaton [b]

[a] *Department of Mechanical and Industrial Engineering, The University of Texas at El Paso, 500 W. University, El Paso, TX 79968-0521, USA*

[b] *Department of Mechanical Engineering, Stanford University, Stanford, CA 94305-3030, USA*

Received 17 November 1999; received in revised form 5 October 2000

Abstract

A developing coaxial swirling jet with sufficient annular swirl for flow recirculation to occur and the effect of the flow field on particle motion were investigated. Experiments were conducted for a single flow condition with a velocity ratio (annular to inner) of 1.15, inner flow Reynolds number of 13,000, swirl number of 0.92 and five particle Stokes numbers ranging from 1 to 5. Instantaneous axial flow visualization illustrated a complex shear layer with a wide range of scales of turbulent motions without easily identifiable quasi-periodic toroidal structures found in non-swirling shear layers. However, toroidal structures amenable to single frequency plane wave excitation were identified, similar to those found in non-swirling shear layers. Using phase-averaged single hot-wire velocity measurements, the toroidal structures in the swirling shear layer were shown to have similar signature to those found in non-swirling shear layers. The instantaneous particle concentration field was measured using digital processing of pulsed laser sheet images. The coherent structures more effectively dispersed particles when compared to the natural jet for the five particle Stokes numbers investigated with the most significant effect occurring for Stokes number near unity. Similar to other single jet results, the particles were preferentially concentrated in the regions between the vortex rings. © 2001 Elsevier Science Ltd. All rights reserved.

Keywords: Swirling recirculating coaxial free jet; Preferential concentration; Particle dispersion; Vortex rings; Forcing

1. Introduction

Swirling jets are utilized in a variety of practical applications. The general effects of swirl on jet development have been known and valued for many years; swirling jets exhibit increased rates of

* Corresponding author. Tel.: +1-915-747-7099; fax: +1-915-747-5019.
E-mail address: rwicker@me.utep.edu (R.B. Wicker).

0301-9322/01/$ - see front matter © 2001 Elsevier Science Ltd. All rights reserved.
PII: S0301-9322(00)00061-6

jet growth, entrainment, and decay of streamwise velocity when compared to their non-swirling counterparts. Perhaps, the most widespread use of swirling flows is in turbulent combustion, where swirl is used for flame stabilization. In strongly swirling jets, the radial and axial pressure gradients are sufficient to cause the flow to recirculate, which stabilizes the flame by matching the flame speed with flow velocity and returning hot combustion products and active chemical species required for ignition back to the flame front. Review articles by Lilley (1977) and Syred and Beér (1974) on swirling flows in combustion systems provide extensive coverage of the general effects of swirl on reacting and non-reacting flowfields.

The current study was motivated by a desire to determine and perhaps control the instantaneous particle concentration field in a coal-fired utility boiler. A common pulverized coal boiler configuration consists of a coal-laden central jet surrounded by one or more swirling annular jets. Over the years, utility boilers have been tuned empirically for high efficiency and low pollutant yield, but further enhancements require a more fundamental approach. In the reaction process, a single particle reacts in a locally fuel-lean environment while a collection of particles reacts in a locally fuel-rich environment. These instantaneous spatial stoichiometry differences affect the overall reaction and pollutant yield. It thus seems desirable to develop an understanding of the instantaneous gas-phase and particle-phase flow fields in this complex flow configuration so that possible combustion control strategies can be developed. In order to achieve this, one must also have an understanding of particle dynamics and particle–fluid interactions.

Several researchers have investigated the instantaneous structure of particle-laden jets and have found the particle concentration field to be strongly affected by the large-scale vortex structures (cf. Longmire and Eaton, 1992). For Stokes numbers between 1 and 10, vortex rings concentrate particles in the high strain rate regions and the cores of the rings are essentially devoid of particles. This phenomenon of turbulence leading to a more organized particle concentration field has become known as "preferential concentration" (Eaton and Fessler, 1994), and is not restricted to flows with simple large-scale structures. Furthermore, the outwardly moving flow in a jet's vortex rings propels particles away from the jet axis, giving the particles "directed motions", or motions strongly correlated with the vortex rings.

The early development of free shear layers is dominated by the natural roll up of vortex rings due to the Kelvin–Helmholtz instability, and the interactions of the rings govern the growth, entrainment, and mixing in these shear layers (cf. Crow and Champagne, 1971). Numerous researchers have studied the response of free shear layers to external perturbations, and demonstrated a wide range of control over the near field vortex structure and dynamics. In single non-swirling jets, slightly perturbing the jet near its preferred mode causes the vortex rings to become regular and periodic. Longmire and Eaton (1992) effectively used this fact to study particle dispersion by superimposing several particle images taken at the same phase in the jet's development. More recently, Aggarwal and Uthuppan (1999) numerically investigated the effects of controlled excitation on particle dispersion in an axisymmetric jet and found higher particle dispersion for all forcing cases analyzed with the most significant effect near unity Stokes numbers. However, similar research with swirling jets has not been performed previously.

Few previous researchers have examined the instantaneous structure of strongly swirling jets, although there have been some recent contributions. Park et al. (1998) used direct numerical simulation to investigate a non-evaporating, droplet-laden swirling jet. They found the large-scale dynamics to be strongly affected by the level of swirl. In strongly swirling jets, the central recir-

culation zone has a dominant effect on the vortex structure. They hypothesize that the vortex structures have a significant effect on the location and size of the recirculation zone. In addition, their results showed that the two phase jet structure and dynamics were affected by both momentum coupling between the phases as well as swirl intensity. For their strongest swirling jet, the droplet-phase caused a significant reduction in the size of the recirculation zone.

Wicker and Eaton (1999) examined the effect of injected longitudinal vorticity on particle dispersion in a swirling coaxial free jet for a single flow condition and particle Stokes number. The jet flow condition examined in Wicker and Eaton (1999) is identical to the one described here, except for strong three-dimensional perturbations injected into the flow using four streamwise vortex generators located at the nozzle exit plane. The vortex generators injected longitudinal vorticity that competed with the mean swirl, causing significant asymmetry in the otherwise axisymmetric toroidal vortex rings and a reduction in the radial particle dispersion. That study was intended to demonstrate that three-dimensionality could be utilized to disrupt the development of large-scale vortex structures characteristic of jets. Longitudinal vortex generators ultimately could be used as a passive particle dispersion control strategy in practical applications.

In the current study, we have investigated particle–fluid interactions in a complex jet flow which resembles a practical particulate fuel jet. This study examined the large-scale, axisymmetric structures that exist in a swirling recirculating flow field (without injected longitudinal vorticity), and the effect of these natural structures on the particle concentration field. We were particularly interested in the effect of instantaneous gas-phase structures, which cause non-uniform dispersion by particle flinging and preferential particle concentration. Our research identified the presence of large-scale vortex rings in the natural jet, similar to those found in non-swirling jets. However, since the natural structures appeared at random times with random spacing, the effects of these structures on the particle concentration field were difficult to quantify. Thus, we used acoustic forcing to organize the vortex ring structure, which enhanced and phase-locked the vortex rings allowing us to perform similar experiments to those presented by Longmire and Eaton (1992) and Wicker and Eaton (1999).

The forced, coaxial swirling jet has many free parameters including the jet Reynolds number, annular/inner velocity ratio, annular/inner diameter ratio, swirl number, and forcing frequency and amplitude. Instead of performing a comprehensive study of the parameter space, we studied a single flow condition and five particle Stokes numbers in detail with the jet parameters in the range characteristic of industrial burners. The forcing was chosen to produce periodic vortex rings similar to the ones found in the natural jet. Similar to Longmire and Eaton (1992), these structures affect the particle concentration field and we believe the observations of preferential concentration by vortex structures in the forced jet are relevant to particle interactions with naturally formed structures in the unforced jet.

2. Experimental facility and techniques

A schematic of the facility and complete details of the experimental techniques can be found in Wicker and Eaton (1994a) and Wicker and Eaton (1999). Briefly, the coaxial jet issued vertically down into ambient fluid through concentric round nozzles with coplanar exits. The inner flow

exited through a 6.45:1 area contraction aluminum nozzle with a 2-cm exit diameter. Swirl was imparted to the annular flow using tangential and axial injectors and flow exited through a 6.30:1 area contraction nozzle with a 6-cm exit diameter. The inner nozzle had a knife-edge exit boundary condition. The annular exit width was 2 cm, yielding an outer-to-inner exit diameter ratio and exit area ratio of 3 and 8, respectively. For all of the work reported here, a single flow condition was used consisting of an inner flow velocity of 10 m/s, inner flow Reynolds number of 13,000, outer-to-inner velocity ratio of 1.15, and swirl number of 0.92 (swirl number is calculated as the axial flux of angular momentum divided by the product of the axial flux of axial momentum and annular nozzle radius). Axial excitation was provided by an audio speaker attached to the top of the annular plenum chamber. Sinusoidal, single frequency forcing was used in all the experiments with an amplitude setting that produced a velocity fluctuation in the outer jet, u'_o/U_o, of 20% measured at the exit plane of the jet (the natural annular jet exit turbulence intensity, u'_o/U_o, was 10%).

Three classes of particles were used (all Ferro Cataphote MS-XL glass shot with different nominal diameters: 55, 90, and 150 μm particles). Size distributions for the particles used in the jet experiments were determined using a Coulter counter. Time scales based on nominal diameters of 55, 90 and 150 μm and Stokes flow are 23, 62 and 172 ms, respectively. Specific data for the experimental conditions and the particles used in the experiments are contained in Tables 1 and 2.

The gas phase was studied using flow visualization, five-hole probe anemometry, and hot-wire anemometry. Flow visualization of smoke-laden flow was utilized to examine both the instantaneous and phase-averaged structure of the jet. Five-hole probe anemometry was used to measure all three mean velocity components and the static pressure. A single hot-wire was used to measure the mean (U) and r.m.s. (u') velocities, the phase-locked streamwise velocity (U_ϕ), and

Table 1
Experimental parameters

U_i	10 m/s
Re_i	13,000
U_o/U_i	1.15
Swirl number, S	0.92
Forcing frequency, f	50, 75 Hz
Strouhal number, St_{Do}	0.26, 0.39
Particle diameter (μm)	55, 90, 150
Stokes number, $St_k = f\tau_p$	1–5

Table 2
Particle properties

Nominal diameter (μm)	55	90	150
Number mean diameter (μm)	55	86.1	149.2
Standard deviation of diameter (μm)	4.6	12.5	7.7
Mass-weighted mean diameter (μm)	55.5	88.4	149.6
Glass density (kg/m^3)	2500	2500	2500
Stokes τ_p (ms)	23.1	61.9	172
Corrected τ_p (ms)	20.6	47.5	100.1

the power spectra of the velocity fluctuations (E_{uu}). The phase-locked velocity provided a useful measure of the strength of the vortex structures, and the power spectra provided useful information for identifying vortex structures amenable to plane wave excitation in the swirling jet shear layer. All these measurements were conventional applications of techniques used for many years in this laboratory.

Numerous objections can be raised to the use of a hot-wire and five-hole probe in a swirling and recirculating flowfield. Certainly, measurements in the recirculating region are subject to large uncertainties due to probe interference (and rectification in the case of the hot-wire). No measurements in the recirculation region using either the hot-wire or five-hole probe are reported here. A detailed database of single-phase flow statistics was not the objective, and thus, the single wire and five-hole probe were used to effectively and quickly obtain information about the gas-phase so that the effect of the gas-phase on the instantaneous particle concentration field could be studied. Total uncertainties for the hot-wire measurements were estimated to be less than 9% for mean and r.m.s. measurements in the majority of the flow for the data reported here. The uncertainty is larger at the edges of the domain where u'/U exceeds 50%. For the five-hole probe, total uncertainties (from flow unsteadiness, instrumentation accuracy, calibration fit, and statistical sources of error) in reported mean velocities are estimated to be less than 4%.

The phase-locked particle concentration field was measured using the technique of Longmire and Eaton (1992). Details of our implementation of this technique are given in Wicker and Eaton (1999). Briefly, the number density was calculated by acquiring multiple images of the particles at fixed forcing phase, locating the centroid of every particle in each image, then fractionally assigning each particle to the four nearest points on a uniform grid. The contribution from each individual particle was normalized by the number of particles found in the image, and the variation in sheet thickness was accounted for to first order by scaling the individual particle concentration by the sheet thickness which was assumed to increase linearly from the waist. Approximately 50 images containing 10,000–40,000 total particles were used in calculating each particle concentration map. Assuming the particle number density distribution for a particular grid follows a Poisson distribution, calculated statistical uncertainties for a 95% confidence interval in particle number density contour levels are $\sim$10% near the jet centerline and as high as 25% near the edge of the jet.

3. Jet qualification

The coaxial nozzles were designed to give nearly top-hat shaped exit axial velocity profiles with low exit turbulence intensities. Mean exit velocity profiles issuing from annular jets have been shown to be strong functions of the swirl number (see Gupta et al., 1984). The mean exit velocity profiles measured using the five-hole probe at $x/D_i = 0.25$ are shown in Fig. 1 (here x is the axial coordinate, r is the radial coordinate, and θ is the azimuthal coordinate. The jet radius and diameter are R and D, respectively, and the subscripts i and o represent inner and outer nozzles, respectively). The profiles were measured along two radial lines separated by 90°. The distributions of axial and azimuthal velocity along the two lines are within 5%.

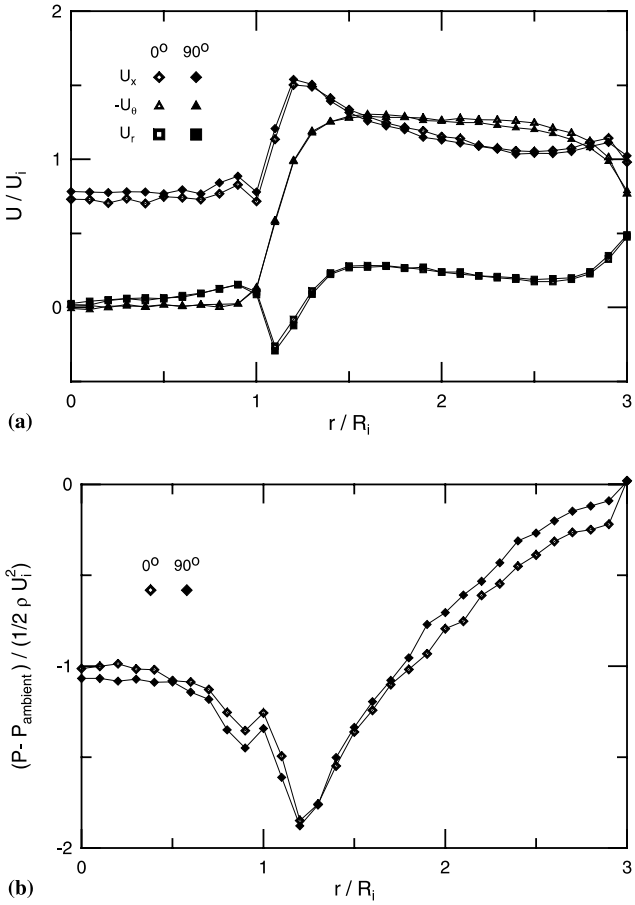

Fig. 1. Swirling coaxial jet qualification: five-hole probe profiles at two jet cross-sections separated by 90° and $x/D_i = 0.25$. (a) Mean velocity; (b) static pressure.

Fig. 1(b) contains the static pressure profiles measured by the five-hole probe at the two jet cross-sections. Due to the azimuthal velocity, the static pressure decreases from ambient pressure at the outer edge of the jet to a minimum at the edge of the shear layer between the annular swirling jet and the inner non-swirling jet. In the shear layer, the static pressure rises slightly as the swirling flow meets the non-swirling flow. This is probably a result of the recirculation zone providing downstream flow blockage which requires rapid radial growth of the inner jet (i.e., axial streamline curvature for the flow exiting the inner jet). The core of the jet has an approximately constant static pressure which is below ambient.

Fig. 2(a) and (b) contain the mean exit velocity and turbulence intensity profiles, respectively, measured with the single hot-wire located 2 mm from the jet exit ($x/D_i = 0.1$). The two mean hot-wire profiles agree within 1%. The relatively large turbulence intensities are produced by tangential injection used to produce swirl. This high turbulence intensity also is characteristic of swirling flows produced by vanes. The high turbulence levels required relatively large forcing amplitudes to phase-lock turbulent structures.

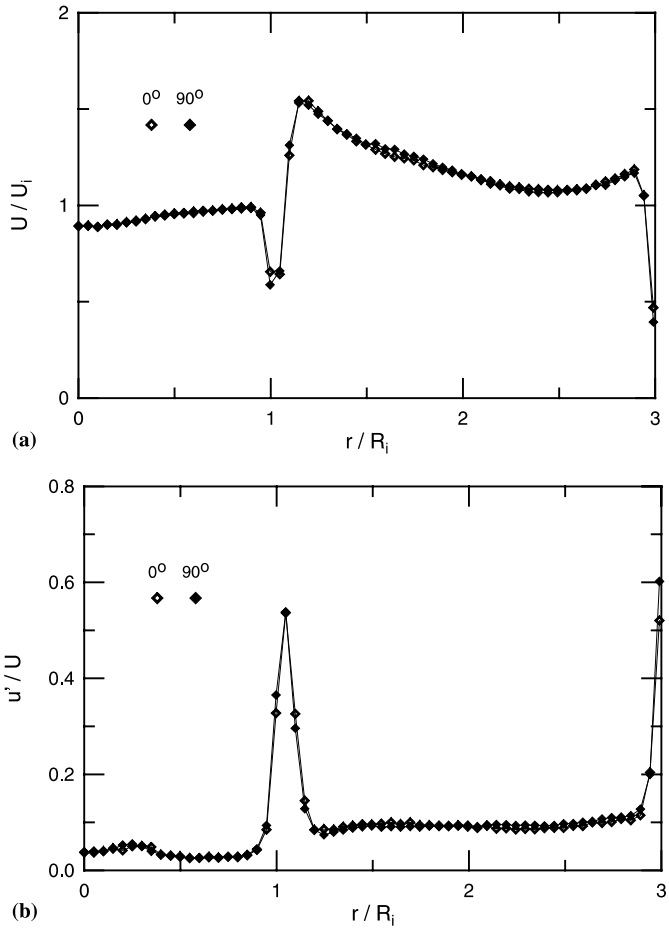

Fig. 2. Swirling coaxial jet qualification: single wire hot-wire profiles at two jet cross-sections separated by 90° and $x/D_i = 0.1$. (a) Mean velocity; (b) turbulence intensity (local r.m.s. velocity normalized by local mean velocity).

4. Results and discussion

4.1. Non-swirling vs. swirling jet structure

Fig. 3 contains instantaneous flow visualization illustrating the effect of swirl on the coaxial jet for an outer-to-inner mean velocity ratio, U_o/U_i, of 1.15, with swirl number, S, of 0 on the left-hand side and S of 0.92 on the right-hand side. Fig. 3(a) shows cases with smoke seeding in the annular jet. The outer shear layer between the annular jet and the ambient for the non-swirling case exhibits the axisymmetric vortex structures found in simple jets. We have previously described the structure of the non-swirling coaxial jet for a variety of velocity ratios (see Wicker and Eaton, 1994a,b). The swirling shear layer exhibits large-scale turbulent motions, but lacks the well-defined axisymmetric structures found in non-swirling cases. In addition, the swirling jet does

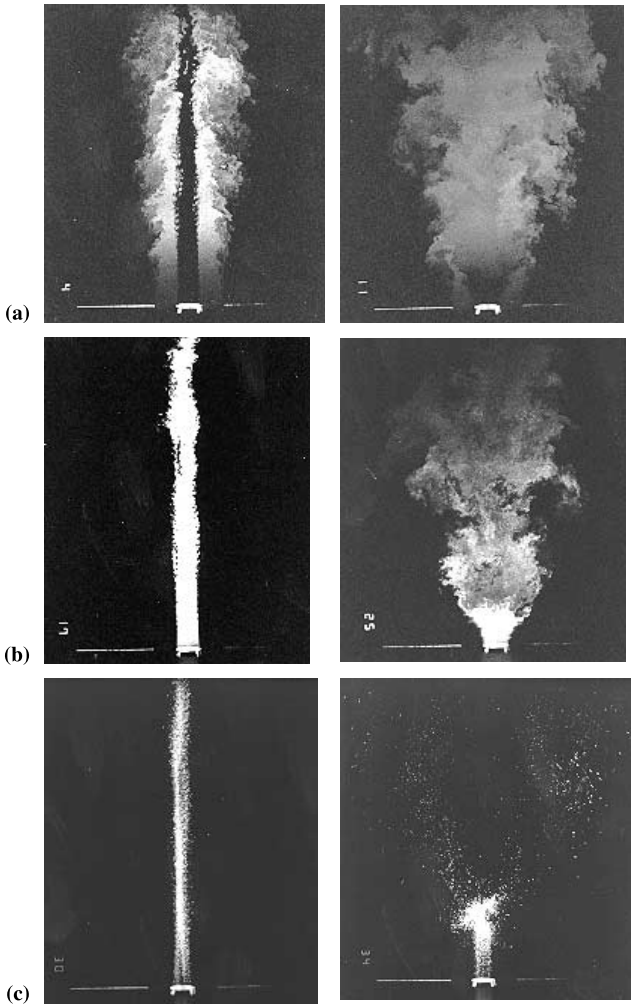

Fig. 3. Non-swirling ($S = 0$) and swirling ($S = 0.92$) jet comparison: (a) annular flow; (b) inner flow; (c) particle concentration field.

not appear to have a potential core region, indicated in the non-swirling jet by higher light intensity in the photograph.

Fig. 3(b) contains the non-swirling and swirling images with inner flow seeding. The non-swirling inner flow has a potential core almost the entire illumination length, indicated by the highest intensity in the photograph. The non-swirling inner layer shows a high frequency instability described previously in Wicker and Eaton (1994b) and begins to meander after about five inner jet diameters. The inner flow meandering is most likely due to an outer or inner layer helical mode. The swirling jet has a very short potential core region extending from the exit of the inner jet to the stagnation point about two inner jet diameters downstream. The rapid deceleration of the inner flow is illustrated by the increased growth rate of the potential core region. After the stagnation point, there appears to be a region of intermediate intensity light. This second region

corresponds to the recirculation zone made up of a mixture of inner and outer flow. After about five inner jet diameters (approximately the end of the recirculation zone), the inner and outer flows have essentially become indiscernible comprising many scales of turbulent motion.

Fig. 3(c) contains the non-swirling and swirling images of the instantaneous particle concentration field for the 55 μm glass beads and approximately 10% particle loading. The non-swirling particle field appears very similar to the inner flow seeded with smoke. There is a high concentration of particles on the jet centerline due to the axisymmetric contraction of the inner and outer flows with an apparent meandering of the particle concentration field downstream. The outer edge has lower concentration finger like particle structures; most likely a result of particle flinging in the shear layer. The swirling particle concentration field has a quite remarkable characteristic. The particles exit the inner contraction and proceed until the recirculating flow provides enough drag to stagnate the particles. This occurs downstream of the gas stagnation point. Most of the particles are then propelled off the axis due to either centrifugal forces or the drag of the diverging flow. The particles are found in bands surrounding the recirculation zone, thus leaving the recirculation zone essentially devoid of particles. This high strain rate stagnation region provides a good example for preferential concentration of particles by turbulence. Similar high concentration was observed by Anderson and Longmire (1995) in a jet stagnating on a wall. In addition, it is interesting to note that the flow visualization provided in Fig. 3 indicates that the initially axisymmetric flow (see Figs. 1 and 2) is maintained for this strongly swirling jet. The jet flow axisymmetry has been confirmed with horizontal flow visualization, which is not shown here for brevity (see Wicker and Eaton, 1994a). This is in distinct contrast to the results of Wicker and Eaton (1999), which showed that injected longitudinal vortices caused strong tilting and distortion of the vortex rings.

4.2. Natural jet development

Mean flow field measurements of the developing jet were made with a five-hole probe in all but the recirculation zone from the jet exit to $x/D_i = 12$. Fig. 4 contains the mean velocity profiles normalized by the bulk inner jet velocity of 10 m/s. The rapid deceleration of the inner flow is evident even by the first-axial station of $x/D_i = 0.20$, where the centerline axial velocity is close to 9 m/s. By $x/D_i = 1.0$, the centerline axial velocity has reduced to approximately 4 m/s. Somewhere between one and two inner jet diameters downstream, the flow stagnates, and by $x/D_i = 2$, the recirculation zone has extended from the centerline to approximately 1.5 inner jet radii. The width of the recirculation zone reaches a maximum of $2R_i$ near $x/D_i = 3$, decreasing to less than $1R_i$ by $x/D_i = 4$. The zone closes somewhere near $x/D_i = 6$, although its effects are evident throughout the measurement region (up to $x/D_i = 12$). Downstream of the recirculation zone, measurements close to the centerline were subject to large uncertainties due to low velocities and high turbulence levels.

In general, the azimuthal velocity behaves as expected; as the jet grows, conservation of angular momentum requires a reduction in azimuthal velocity. The large azimuthal velocities at the exit plane (approximately 12.5 m/s) have reduced to about 2 m/s by $x/D_i = 12$. The radial velocities are also provided in the figure. Close to the jet exit, the outer part of the jet is growing rapidly, indicated by large radial velocities. At the first measurement location ($x/D_i = 0.2$), the inner jet is also growing rapidly. At $x/D_i = 1$, radial velocities exceed 5 m/s in the outer portion of the jet. At

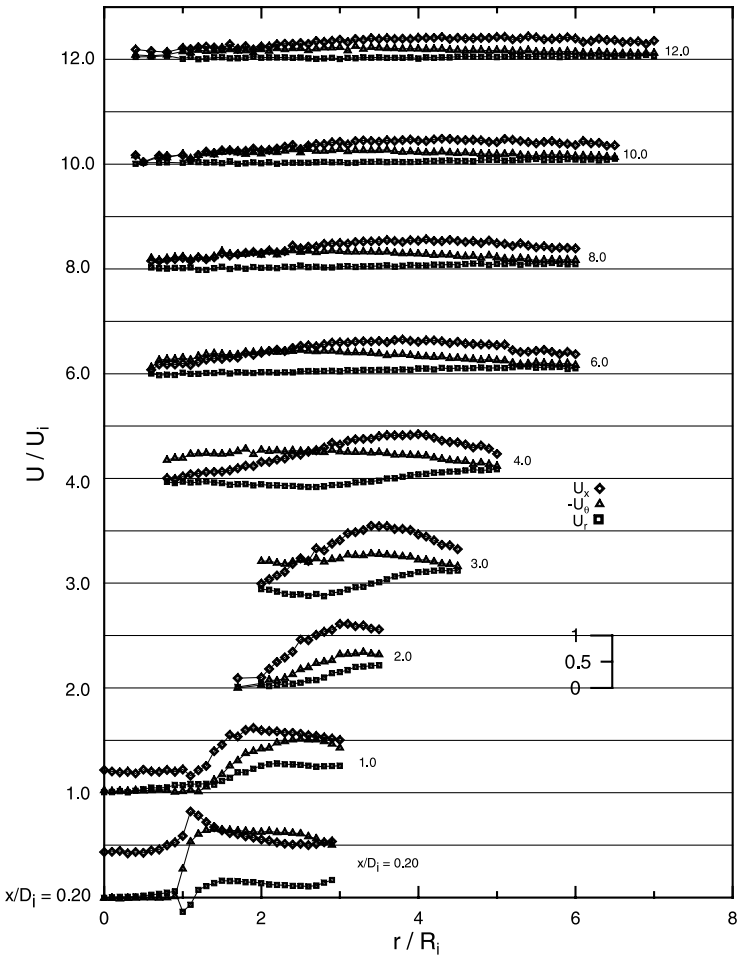

Fig. 4. Natural swirling coaxial jet development: five-hole probe mean velocities.

$x/D_i = 3$ and $x/D_i = 4$, the recirculation zone is closing, requiring negative radial velocities and by $x/D_i = 12$, radial velocities have reduced to less than 1 m/s.

The static pressure profiles were also measured with the five-hole probe, although they are not shown here for brevity (see Wicker and Eaton, 1994a). The largest pressure difference is measured at the first measurement location, as shown in Fig. 2(b) and described previously. After this location, the jet grows and the static pressure approaches ambient pressure and by $x/D_i = 12$, the static pressure is nearly uniform.

The single wire, despite its shortcomings, provided much useful information. Fig. 5 contains single wire profiles at several downstream locations for the natural jet and the forced jet for two forcing conditions (the forced jet will be discussed later). The single wire was oriented such that the axis of the wire was aligned with the tangential direction, eliminating any sensitivity to the azimuthal velocity component. Thus, the single wire measured an effective cooling velocity equal to the vector sum of the axial and radial velocities. In regions where the radial velocities were

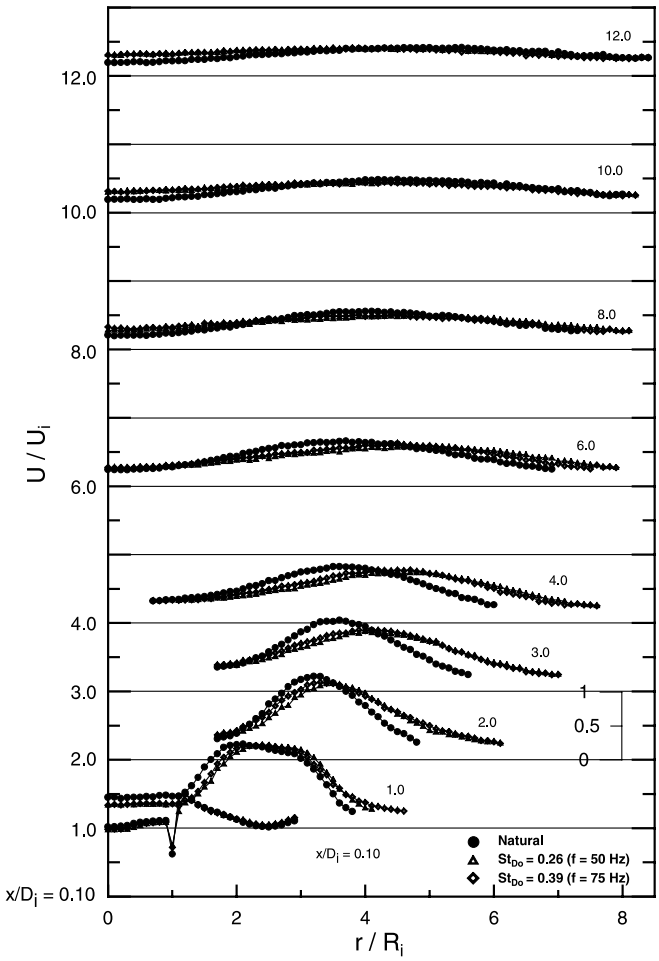

Fig. 5. Axially excited and natural swirling coaxial jet single hot-wire mean velocities.

small, the single wire velocities (in Fig. 5) and five-hole probe axial velocities (in Fig. 4) are essentially indiscernible. In regions where the radial velocity was large, the single wire measured a velocity only slightly larger than the axial velocity because in general, the axial velocities were at least a factor of two larger than the radial velocities.

To obtain the data shown in Fig. 5, the hot-wire was traversed from the jet centerline until a velocity of 2.5 m/s was obtained. Therefore, the outermost point in the hot-wire profiles can be used as an indication of jet growth. Up to $x/D_i = 3$, the jet grows rapidly; growing approximately 3 cm in radius by $x/D_i = 3$. After the initial rapid growth region, the growth rate decreases, with the jet reaching ~7.5 cm in radius at $x/D_i = 8$. The effect of the recirculation zone is still apparent at $x/D_i = 12$, although the profile seems to be approaching a single jet similarity solution.

Fig. 6 shows the measured turbulence intensity profiles at several axial locations for the natural jet and the two forced jets. Turbulence production is extremely high in this flow field and by $x/D_i = 1$, turbulence intensities in the outer part of the natural jet have exceeded 30%. Hot-wire

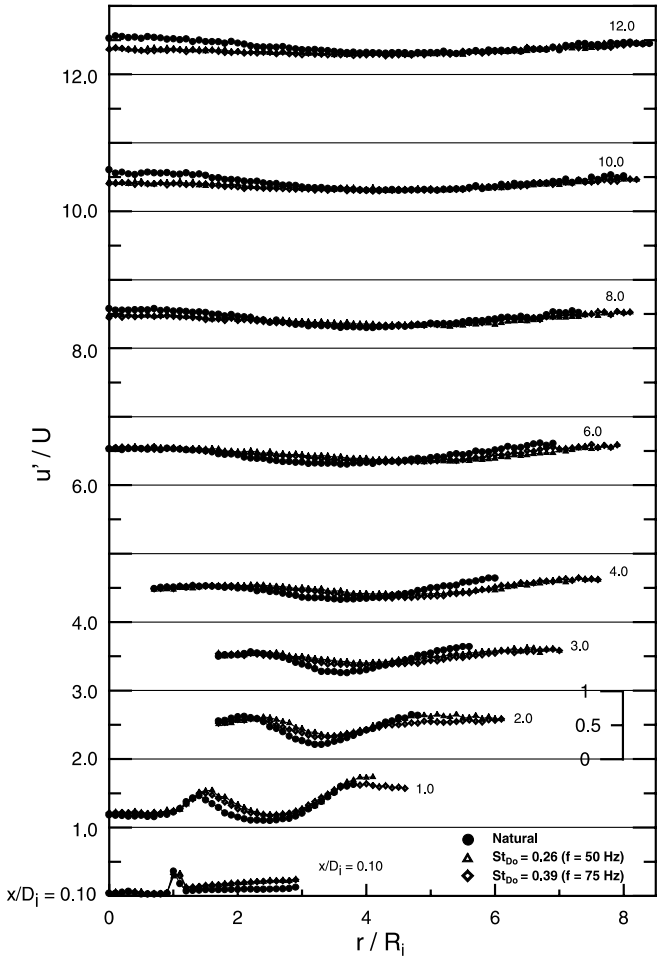

Fig. 6. Axially excited and natural swirling coaxial jet single wire hot-wire turbulence intensities (local r.m.s. velocity normalized by local mean velocity).

measurements are subject to large uncertainties in high turbulence regions, and the turbulence levels remain high throughout the flow field. The turbulence profiles have two peaks associated with the inner and outer shear layers. These peaks spread and decrease in intensity going downstream. By $x/D_i = 8$, the entire jet is at relatively high turbulence intensity, although the two shear layer peaks are still evident.

4.3. Swirling jet with forcing

Flow visualization showed large-scale turbulent motions in the swirling jet with a range of sizes. The presence of large-scale eddies was clear in instantaneous particle concentration images, but it was not known if the eddies had a characteristic frequency, and if so, what this characteristic frequency was. Detailed discussion of how we identified frequencies amenable to plane wave

excitation in the swirling shear layer is contained in Wicker and Eaton (1994a). As a result of our studies, we identified two forcing conditions, $f = 50$ Hz and $f = 75$ Hz, corresponding to Strouhal numbers (St_{Do}) of 0.26 and 0.39, respectively, based on outer jet diameter and bulk outer axial exit velocity that produced axisymmetric toroidal vortex rings similar to those found in non-swirling jets. We base the conclusion that the structures in the swirling shear layer are similar to those present in non-swirling shear layers on several measurements which are detailed below.

Figs. 7 and 8 contain measured single wire hot-wire spectra at seven axial locations for the forcing frequencies of 50 and 75 Hz, respectively. In Fig. 7, the 50 Hz forcing appears in the spectra up to $x/D_{\mathrm{i}} = 10$, but by $x/D_{\mathrm{i}} = 8$, the energy at 50 Hz is below the lower frequency energy. For locations upstream of $x/D_{\mathrm{i}} = 8$, there appears to be a strong organization of energy around the forcing frequency. The first harmonic also appears in the spectra from $x/D_{\mathrm{i}} = 1.0$ to $x/D_{\mathrm{i}} = 4$, with apparent amplification from $x/D_{\mathrm{i}} = 1$ to $x/D_{\mathrm{i}} = 2$. For the 75 Hz forcing, shown in Fig. 8,

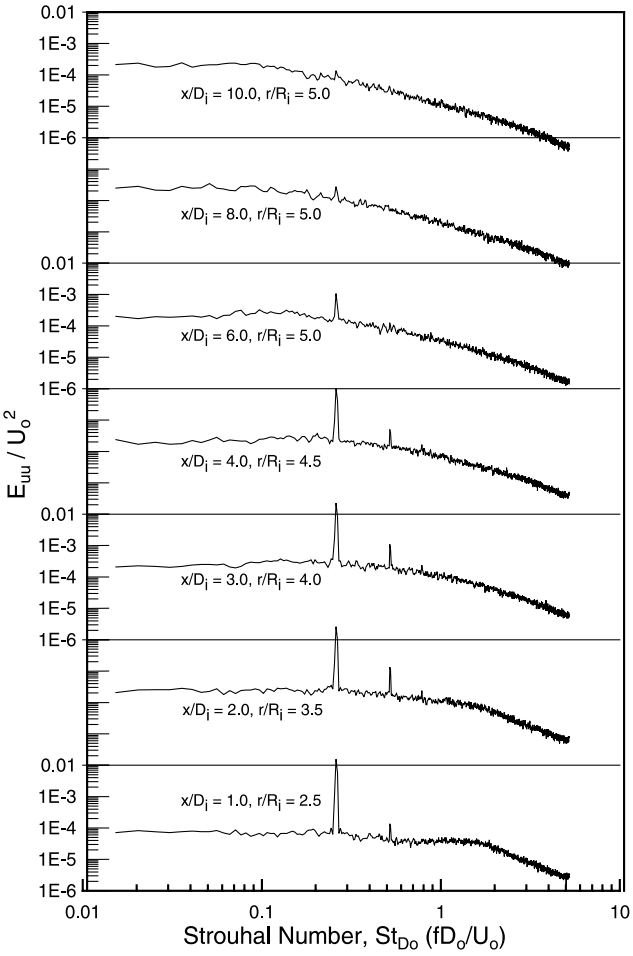

Fig. 7. Axially excited swirling coaxial jet single wire hot-wire power spectra of the velocity fluctuations ($St_{\mathrm{Do}} = 0.26$, $f = 50$ Hz).

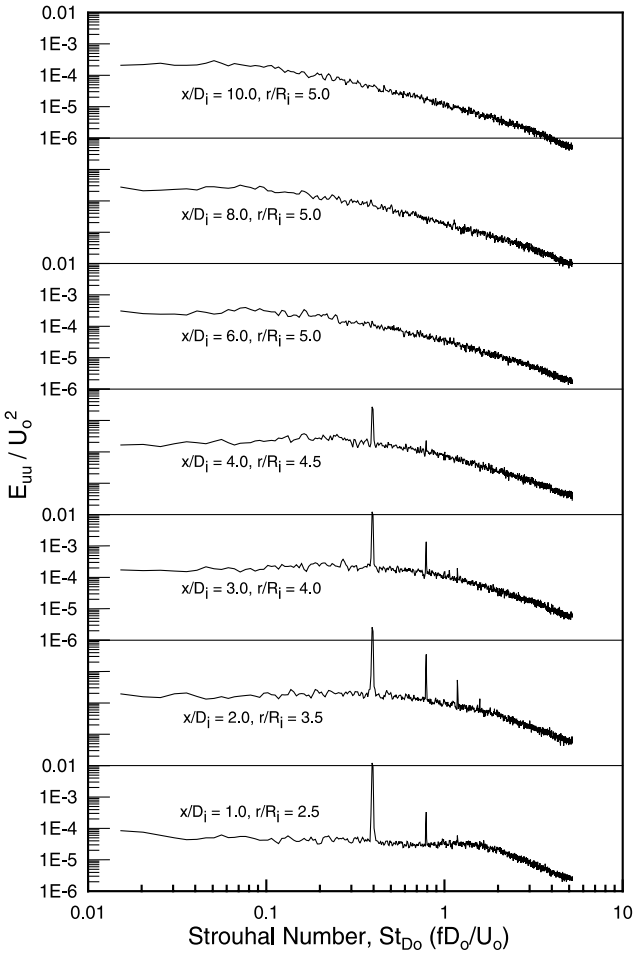

Fig. 8. Axially excited swirling coaxial jet single wire hot-wire power spectra of the velocity fluctuations ($St_{\mathrm{Do}} = 0.39$, $f = 75$ Hz).

there also appears to be an organization of energy around the forcing frequency, but by $x/D_{\mathrm{i}} = 6$, the effects of the forcing have diminished. The first harmonic also appears in the spectra from $x/D_{\mathrm{i}} = 1$ to $x/D_{\mathrm{i}} = 4$, with an amplification from $x/D_{\mathrm{i}} = 1$ to $x/D_{\mathrm{i}} = 2$ (the second and third harmonics also appear in the spectrum at $x/D_{\mathrm{i}} = 2$). The natural spectra have not been included for brevity. They are similar to the forced spectra, except without concentrated energy at the forcing frequency (cf. Wicker and Eaton, 1994a).

Phase-averaged hot-wire measurements were obtained to help characterize the vortex structures. The single wire hot-wire was used to take phase-averaged velocity profiles using 500 points in the velocity calculation. The phase-averaged velocity data were plotted on spatial vector plots including contours of constant velocity. Note that the information in the vector and contour plots is redundant since only a single velocity component was measured.

A single axisymmetric jet was examined first to understand how a series of vortex rings would appear using this type of measurement. Fig. 9 contains the vector and contour plots for a single jet

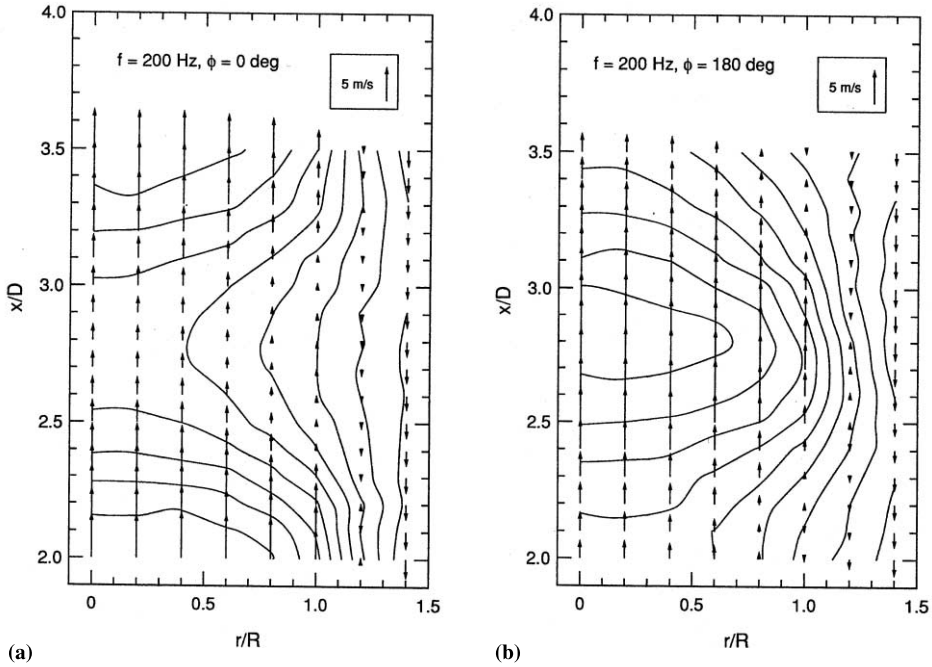

Fig. 9. Phase-averaged single jet velocity vector and contour maps from single wire hot-wire measurements ($St_{Do} = 0.4$): (a) $\phi = 0°$; (b) $\phi = 180°$.

forced at a Strouhal number of 0.4 and two different phases in the forcing cycle $\phi = 0°$ and 180°. An assumed convection velocity of 5 m/s has been subtracted from the velocity vectors. These plots quite clearly show the signature for a series of vortex rings measured by a single wire hot-wire. For $\phi = 0°$, the vortex ring is located at approximately $x/D = 1.5$, $r/R = 1.1$ and $x/D = 3.1$, $r/R = 1.1$, each with a radius of about 1/2 jet diameter, measured from flow visualization. The contours that extend from the outer part of the shear layer toward the axis and then return to the outer part of the shear layer with increasing x/D, provide a characteristic signature for the saddle region between vortex rings. In Fig. 9(b) taken at $\phi = 180°$, there is only a single vortex located at approximately $x/D = 2.3$, $r/R = 1.1$, again with a radius of approximately 1/2 jet diameter. Comparison of the location of the vortices in Fig. 9 shows that iso-velocity contours do not necessarily follow the direction of flow in the vortex rings. However, the vortex rings are near large velocity gradients characterized by closely spaced contours.

Fig. 10 contains the single wire hot-wire phase-averaged vector and contour plots for the swirling jet with $f = 50$ Hz ($St_{\mathrm{Do}} = 0.26$) and $\phi = 0°$ and 180°. For $\phi = 0°$ (Fig. 10(a)), the signature for a saddle region is identified from approximately $x/D_{\mathrm{i}} = 3.5$ to $x/D_{\mathrm{i}} = 5$. From flow visualization (to be discussed below), a structure appears to be located at $x/D_{\mathrm{i}} = 1.8$, $r/R_{\mathrm{i}} = 3.5$ with a diameter of approximately $1.5D_{\mathrm{i}}$. A second vortex is located approximately at $x/D_{\mathrm{i}} = 6$, $r/R_{\mathrm{i}} = 5.5$ with a diameter of approximately $2D_{\mathrm{i}}$. Therefore, the signature saddle region contour correctly identifies the saddle region in the swirling jet. Similar comparisons can be made between flow visualization and phase-averaged hot-wire data for $\phi = 180°$. Additional results for the 75 Hz forcing frequency and more phases in the forcing cycle can be found in Wicker and Eaton (1994a).

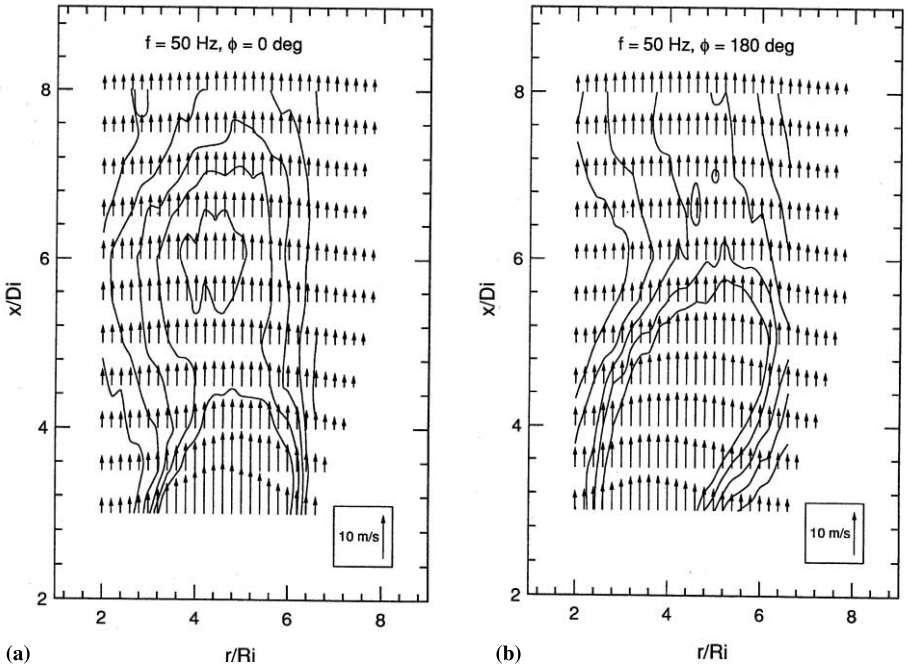

Fig. 10. Phase-averaged swirling coaxial jet velocity vector and contour maps from single wire hot-wire measurements ($St_{\mathrm{Do}} = 0.26$, $f = 50$ Hz): (a) $\phi = 0°$; (b) $\phi = 180°$.

Phase-locked flow visualization of smoke seeded flow was also performed to help determine if the forcing produced axisymmetric toroidal vortex rings similar to those found in single jets. The laser was triggered at the forcing frequency and a specified phase in the forcing cycle and a number of phase-locked laser pulses occurred while the camera shutter was open (typically, 12 pulses per photograph). These images are contained in Fig. 11 along with the unforced jet (visualized in the same manner) as a basis for comparison. The laser sheet originates on the right and is expanding from right to left, accounting for the lower intensity in the left half plane. The two large white dots located to the left of the jet were two pins separated by 3 cm that intersected the light sheet used for scale reference. Fig. 11(a) should be compared to Fig. 3, an instantaneous view of the unforced jet. The large-scale structures visible in Fig. 3 are not apparent in Fig. 11(a) due to the averaging.

Fig. 11(b) shows the phase-averaged images for the 50 Hz forcing frequency ($St_{\mathrm{Do}} = 0.26$) and a phase angle, ϕ, of 0°and 180°. There are two axisymmetric structures evident (see arrows) after which the jet appears similar to the natural jet. In all of the images obtained, the axisymmetric structure remains coherent for approximately two structure wavelengths prior to breaking down.

The phase-averaged images for 75 Hz forcing ($St_{\mathrm{Do}} = 0.39$) are shown in Fig. 11(c) for ϕ of 0°and 180°. Again, the images illustrate the large-scale vortical structures phase-locked by the forcing. These structures also appear to remain coherent for approximately two structure wavelengths. The structure appears to survive until $x/D_{\mathrm{i}} = 6.5$, based on the $\phi = 180°$ case, before

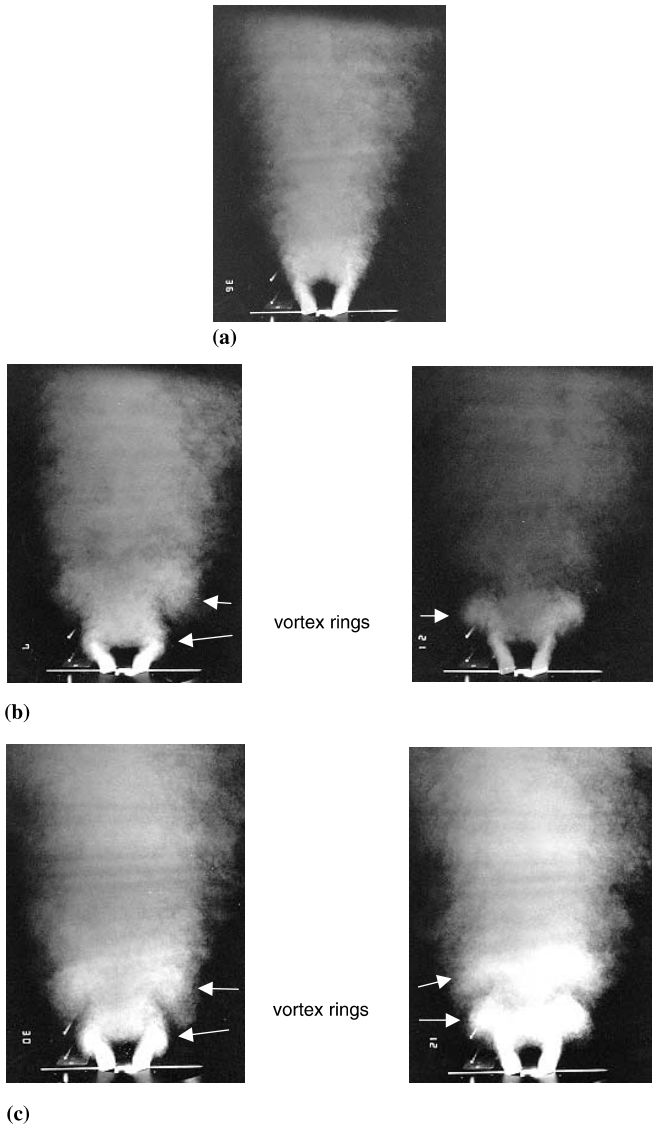

Fig. 11. Phase-averaged flow visualization: (a) natural jet (time-averaged); (b) $St_{Do} = 0.26$ ($f = 50$ Hz), $\phi = 0°$ and 180°; (c) $St_{Do} = 0.39$ ($f = 75$ Hz)), $\phi = 0°$ and 180°.

ultimately losing coherence. Note that the vortex rings are more closely spaced with the higher frequency excitation.

4.4. Forced jet development

The mean velocity profiles for the two forced jets are shown in Fig. 5. At $x/D_i = 1$, using the minimum velocity of 2.5 m/s as the growth indicator, the 75 Hz forced jet has grown to $r/R_i = 4.6$

and the 50 Hz forced jet has grown to $r/R_i = 4.1$, while the natural jet is at $r/R_i = 3.8$. By $x/D_i = 2$, the 50 Hz jet has caught up to the 75 Hz jet where they are both at approximately $r/R_i = 6$ and by $x/D_i = 6$, the 50 Hz jet has surpassed the 75 Hz jet by about 4 mm ($r/R_i = 7.9$ and $r/R_i = 7.5$, respectively with the natural jet at $r/R_i = 6.9$). By $x/D_i = 10$, the natural jet has nearly caught up to the forced jets and by $x/D_i = 12$, the outer portion of the three jets are nearly indiscernible. The velocity near the centerline for the forced jets is slightly larger than the natural jet, with the forced jet profiles approaching similarity more quickly.

The measured turbulence intensity profiles for the two forced jets are shown in Fig. 6. Turbulence levels for the forced jets are similar to the natural jet with the profiles shifted radially due to differences in jet growth. Further evidence that the forced jets have more closely achieved similarity is provided at $x/D_i = 12$, where turbulence intensities still exceed 30% but appear to be below the natural jet levels. It is apparent from these data that the forcing serves to organize the existing structure without making gross changes to the statistical behavior of the jet.

4.5. Particle concentration field

Contours of normalized number density for the unforced jet and the three particle sizes are plotted in Fig. 12. When compared to the smoke flow visualization, the contour signature exhibits similar characteristics to the particle images. The high concentration stagnation region is clearly visible in the figure, along with the bands of particles propelled off the axis due to centrifugal forces or the drag of the diverging flow. However, there are several differences that can be noted upon comparison of the natural jet laden with 55, 90, or 150 μm particles. In general, the smaller particles appear more dispersed radially and toward the centerline than the larger particles. If the

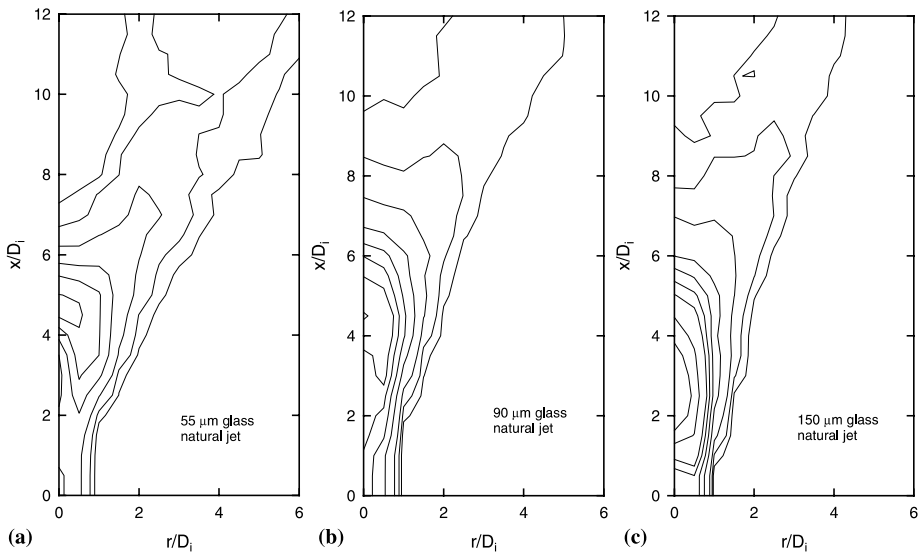

Fig. 12. Time-averaged swirling coaxial jet normalized particle number density, no forcing, laser triggered at 50 Hz. Contour levels: 0.0005, 0.001, 0.002, 0.004, 0.006, 0.008, 0.01, 0.015, 0.02. (a) 55 μm glass; (b) 90 μm glass; (c) 150 μm glass.

lowest contour level is used to calculate a particle concentration width, the 55 μm jet has a width of approximately $5.5D_i$ at $x/D_i = 10$, the 90 μm jet is approximately $4D_i$ wide at $x/D_i = 10$, and the 150 μm jet is approximately $3.75D_i$ wide at $x/D_i = 10$. Furthermore, the effect of the higher inertia particles can be seen by longer and thinner high concentration regions for the larger particles.

Fig. 13 contains normalized and phase-averaged particle concentration maps for the three particle sizes and the 50 Hz ($St_{Do} = 0.26$) forcing condition. All particle sizes appear to respond to the forcing condition, as indicated in the figure. The lowest contour level has grown radially outward into the quiescent fluid and also toward the centerline with the most significant effect of the forcing on the smallest particles. That is, the forcing more effectively disperses the particles. In addition, in all of the images, the forced jet lowest contour is not "smooth"; instead, it has an apparent waviness. We believe this waviness is an indication of preferential concentration of these particles due to the flow structures. Both increased particle dispersion and preferential particle concentrations are discussed in more detail below.

To demonstrate the differences in particle dispersion between the forced jet and the natural jet, contours of particle number density differences have been calculated where the normalized particle number density in the natural jet has been subtracted from its corresponding grid location in the forced jet. Thus, regions containing more particles in the forced jet have positive contours (solid lines) while regions where the natural jet contains more particles have negative (dashed lines) contours. In Fig. 14, the particle subtraction contours are shown for the natural jet subtracted from the forced jet ($St_{Do} = 0.26$, $f = 50$ Hz) with $\phi = 0^\circ$ for the three particle sizes. The figure clearly shows that the forced jet has dispersed more particles radially for all three particle sizes. For the 55 μm particles, the forced jet also has a region near the jet centerline with higher particle

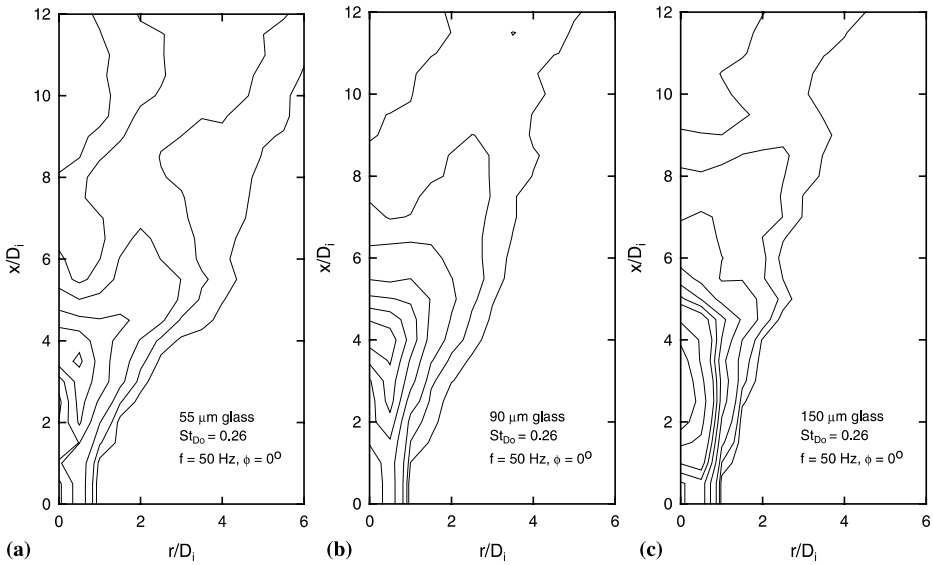

Fig. 13. Phase-averaged swirling coaxial jet normalized particle number density, $St_{Do} = 0.26$ (50 Hz forcing), $\phi = 0°$, laser triggered at 50 Hz. Contour levels: 0.0005, 0.001, 0.002, 0.004, 0.006, 0.008, 0.01, 0.015, 0.02. (a) 55 μm glass; (b) 90 μm glass; (c) 150 μm glass.

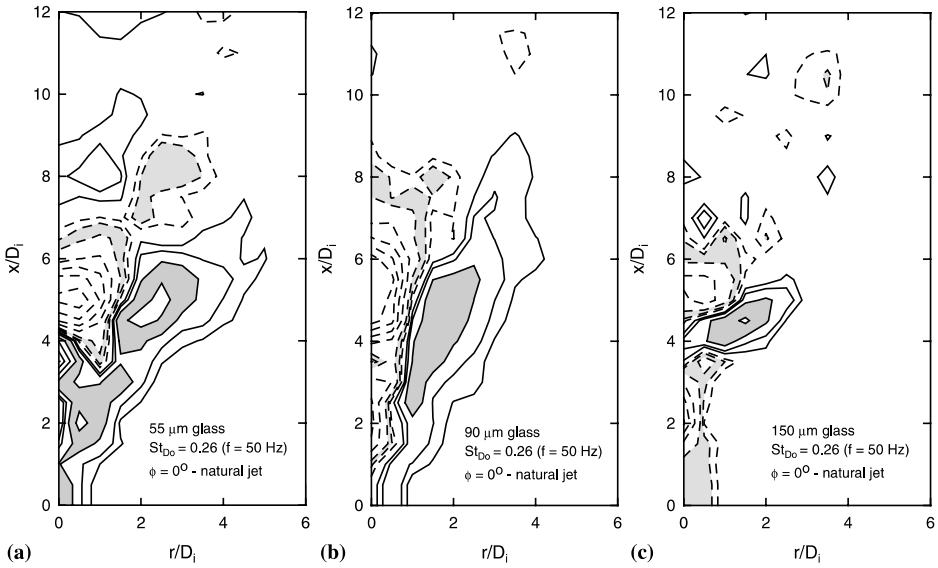

Fig. 14. Normalized particle number density subtractions for the phase-averaged forced jet minus the time-averaged natural jet, $St_{\mathrm{Do}} = 0.26$ (50 Hz forcing), $\phi = 0°$, laser triggered at 50 Hz. Contour levels: ±0.00025, 0.0005, 0.001, 0.002, 0.003, 0.004, and 0.005. Area enclosed by third lowest contour level (±0.001) is shaded for convenience. (a) 55 μm glass; (b) 90 μm glass; (c) 150 μm glass.

concentrations than the natural jet. In addition, all of the figures show one or more high concentration regions off the axis in the forced jet. From the flow visualization for $St_{\mathrm{Do}} = 0.26$ ($f = 50$ Hz, $\phi = 0^{\circ}$) shown in Fig. 11(b), one vortex appears to be located at $x/D_{\mathrm{i}} = 1.8$, $r/D_{\mathrm{i}} = 1.75$ with a diameter of approximately $1.5D_{\mathrm{i}}$ and the second vortex is approximately at $x/D_{\mathrm{i}} = 6$, $r/D_{\mathrm{i}} = 2.75$ with a diameter of approximately $2D_{\mathrm{i}}$. Thus, the high particle concentration region located near $x/D_{\mathrm{i}} = 4.5$ for all of the particle sizes appears to lie directly between the vortex rings. This is in agreement with the observations of Longmire and Eaton (1992) in a much simpler jet.

5. Conclusions

The near field of circular, non-swirling jets is dominated by vortex rings whose interactions govern the growth, entrainment, and mixing in the jet. Controlled perturbations can cause major changes in the overall behavior of the jet by organizing the vortex rings in the jet near field. The interaction of particles with these structures is important in particle and spray combustion with implications in combustion control. It has been shown previously that the particles in the near field of a single round jet accumulate in the regions between vortex rings and are propelled away from the jet axis by the outwardly moving flow in these regions.

The present results indicate that large-scale vortex rings are present and have similar effects on the particle distribution in a much more complicated jet that includes a coaxial swirling flow with sufficient swirl to establish a central recirculation zone. Instantaneous smoke flow visualization of

the natural swirling jet shows the presence of large vortex structures and a non-uniform concentration distribution such as might be produced by vortex rings. Simple single frequency axial excitation of the annular flow produces repeatable, axisymmetric vortex structures in the near field. Relatively large (20%) forcing is required to phase-lock the structures, probably because of the high turbulence in the swirling jet inflow or because of the high turbulence levels fed back to the near field via the recirculation region. The most coherent response to forcing is found for a forcing Strouhal number of 0.26 based on the outer jet diameter and bulk axial exit velocity.

The phase-locked vortex structures have a significant effect on the particle concentration field for all particle Stokes numbers tested ranging from 1 to 5. Radial dispersion due to the vortex structures is strongest for the lightest particles studied, although in all cases, the vortices enhance the radial dispersion as compared to the natural jet. Forcing of the jet preferentially concentrates the particles into relatively narrow bands with concentration peaks occurring in the saddle regions between vortex rings. Again, this preferential concentration occurs for all Stokes numbers tested. Wicker and Eaton (1999) showed that longitudinal vortices injected at the nozzle could distort the vortex rings markedly reducing the concentration peaks and the particle radial dispersion. The present work shows that the axisymmetric rings are quite robust. In the absence of strong coherent three-dimensional perturbations such as those used by Wicker and Eaton (1999), the axisymmetric rings play a very strong role, even in the highly turbulent swirling jet field.

Preferential particle concentrations, in and of themselves, are not necessarily undesirable. In fact, from a coal combustion standpoint, conversion of nitrogen containing species to NO_x is reduced for fuel-rich combustion, or for preferentially concentrated coal. However, these results indicate that for the Stokes numbers investigated, preferential particle concentrations are associated with large-scale structures which more effectively disperse the particles and cause directed particle motions. As a result, a single particle that has been thrown beyond the flame sheet will react in a locally fuel-lean environment, and ultimately, contribute to pollutant yield. Thus, single frequency axial excitations do not appear to be an effective means for coal combustion pollution control. However, aerodynamic passive control alternatives exist which may prove to be extremely useful in mitigating coal combustion environmental impacts (see Wicker and Eaton, 1999).

Acknowledgements

This work was funded by the Electric Power Research Institute under Contract No. RP 8005-02 monitored by Dr. George Offen.

References

Aggarwal, S.K., Uthuppan, J., 1999. Particle dispersion enhancement in the near region of a forced jet. Journal of Propulsion and Power 15, 266–271.

Anderson, S.L., Longmire, E.K., 1995. Particle motion in the stagnation zone of an impinging air jet. Journal of Fluid Mechanics 299, 333–366.

Crow, S.C., Champagne, F.H., 1971. Orderly structure in jet turbulence. Journal of Fluid Mechanics 48, 547–591.

Eaton, J.K., Fessler, J.R., 1994. Preferential concentration of particles by turbulence. International Journal of Multiphase Flow 20 (Suppl.), 169–209.

Gupta, A.K., Lilley, D.G., Syred, N., 1984. Swirl Flows. Abacus Press, Tunbridge Wells, Kentucky.

Longmire, E.K., Eaton, J.K., 1992. Structure of a particle-laden round jet. Journal of Fluid Mechanics 236, 217–257.

Lilley, D.G., 1977. Swirl flows in combustion: A review. AIAA Journal 15, 1063–1078.

Park, T.W., Katta, V.R., Aggarwal, S.K., 1998. On the dynamics of a two-phase non-evaporating swirling jet. Int. J. Multiphase Flow 24, 295–317.

Syred, N., Beér, J.M., 1974. Combustion in swirling flows: A review. Combustion and Flame 23, 143–201.

Wicker, R.B., Eaton, J.K., 1994a. Structure and Control of a Particle-Laden Coaxial Jet With and Without Annular Swirl, Report MD-68, Thermosciences Division, Department of Mechanical Engineering, Stanford University.

Wicker, R.B., Eaton, J.K., 1994b. Near field of a coaxial jet with and without axial excitation. AIAA Journal 32, 542–546.

Wicker, R.B., Eaton, J.K., 1999. Effect of injected longitudinal vorticity on particle dispersion in a swirling coaxial jet. Journal of Fluids Engineering 121, 766–772.